BICEP2 / *Keck Array* **VI: Improved Constraints On Cosmology and Foregrounds When Adding 95 GHz Data From** *Keck Array*

Keck Array and BICEP2 Collaborations: P. A. R. Ade,[1] Z. Ahmed,[2,3] R. W. Aikin,[4] K. D. Alexander,[5] D. Barkats,[5] S. J. Benton,[6] C. A. Bischoff,[5] J. J. Bock,[4,7] R. Bowens-Rubin,[5] J. A. Brevik,[4] I. Buder,[5] E. Bullock,[8] V. Buza,[5,9] J. Connors,[5] B. P. Crill,[7] L. Duband,[10] C. Dvorkin,[9] J. P. Filippini,[4,11] S. Fliescher,[12] J. Grayson,[3] M. Halpern,[13] S. Harrison,[5] G. C. Hilton,[14] H. Hui,[4] K. D. Irwin,[3,2,14] K. S. Karkare,[5] E. Karpel,[3] J. P. Kaufman,[15] B. G. Keating,[15] S. Kefeli,[4] S. A. Kernasovskiy,[3] J. M. Kovac,[5,9,*] C. L. Kuo,[3,2] E. M. Leitch,[16] M. Lueker,[4] K. G. Megerian,[7] C. B. Netterfield,[6,17] H. T. Nguyen,[7] R. O'Brient,[4,7] R. W. Ogburn IV,[3,2] A. Orlando,[4,15] C. Pryke,[12,8,†] S. Richter,[5] R. Schwarz,[12] C. D. Sheehy,[12,16] Z. K. Staniszewski,[4,7] B. Steinbach,[4] R. V. Sudiwala,[1] G. P. Teply,[4,15] K. L. Thompson,[3,2] J. E. Tolan,[3] C. Tucker,[1] A. D. Turner,[7] A. G. Vieregg,[5,18,16] A. C. Weber,[7] D. V. Wiebe,[13] J. Willmert,[12] C. L. Wong,[5,9] W. L. K. Wu,[3] and K. W. Yoon[3,2]

[1]*School of Physics and Astronomy, Cardiff University, Cardiff, CF24 3AA, United Kingdom*
[2]*Kavli Institute for Particle Astrophysics and Cosmology,*
SLAC National Accelerator Laboratory, 2575 Sand Hill Rd, Menlo Park, California 94025, USA
[3]*Department of Physics, Stanford University, Stanford, California 94305, USA*
[4]*Department of Physics, California Institute of Technology, Pasadena, California 91125, USA*
[5]*Harvard-Smithsonian Center for Astrophysics, 60 Garden Street MS 42, Cambridge, Massachusetts 02138, USA*
[6]*Department of Physics, University of Toronto, Toronto, Ontario, M5S 1A7, Canada*
[7]*Jet Propulsion Laboratory, Pasadena, California 91109, USA*
[8]*Minnesota Institute for Astrophysics, University of Minnesota, Minneapolis, Minnesota 55455, USA*
[9]*Department of Physics, Harvard University, Cambridge, MA 02138, USA*
[10]*Service des Basses Températures, Commissariat à l'Energie Atomique, 38054 Grenoble, France*
[11]*Department of Physics, University of Illinois at Urbana-Champaign, Urbana, Illinois 61801, USA*
[12]*School of Physics and Astronomy, University of Minnesota, Minneapolis, Minnesota 55455, USA*
[13]*Department of Physics and Astronomy, University of British Columbia,*
Vancouver, British Columbia, V6T 1Z1, Canada
[14]*National Institute of Standards and Technology, Boulder, Colorado 80305, USA*
[15]*Department of Physics, University of California at San Diego, La Jolla, California 92093, USA*
[16]*Kavli Institute for Cosmological Physics, University of Chicago, Chicago, IL 60637, USA*
[17]*Canadian Institute for Advanced Research, Toronto, Ontario, M5G 1Z8, Canada*
[18]*Department of Physics, Enrico Fermi Institute, University of Chicago, Chicago, IL 60637, USA*

We present results from an analysis of all data taken by the BICEP2 & *Keck Array* CMB polarization experiments up to and including the 2014 observing season. This includes the first *Keck Array* observations at 95 GHz. The maps reach a depth of 50 nK deg in Stokes Q and U in the 150 GHz band and 127 nK deg in the 95 GHz band. We take auto- and cross-spectra between these maps and publicly available maps from WMAP and *Planck* at frequencies from 23 GHz to 353 GHz. An excess over lensed-ΛCDM is detected at modest significance in the 95×150 BB spectrum, and is consistent with the dust contribution expected from our previous work. No significant evidence for synchrotron emission is found in spectra such as 23×95, or for dust/sync correlation in spectra such as 23×353. We take the likelihood of all the spectra for a multi-component model including lensed-ΛCDM, dust, synchrotron and a possible contribution from inflationary gravitational waves (as parametrized by the tensor-to-scalar ratio r), using priors on the frequency spectral behaviors of dust and synchrotron emission from previous analyses of WMAP and *Planck* data in other regions of the sky. This analysis yields an upper limit $r_{0.05} < 0.09$ at 95% confidence, which is robust to variations explored in analysis and priors. Combining these B-mode results with the (more model-dependent) constraints from *Planck* analysis of CMB temperature and other evidence yields a combined limit $r_{0.05} < 0.07$ at 95% confidence. These are the strongest constraints to date on inflationary gravitational waves.

Introduction.—Measurements of the cosmic microwave background (CMB) [1] are one of the observational pillars of the standard cosmological model (ΛCDM) and constrain its parameters to high precision (see most recently Ref. [2]). This model extrapolates the Universe back to very high temperatures ($\gg 10^{12}$ K) and early times. Observations indicate that conditions at early times are described by an almost uniform plasma with a nearly scale invariant spectrum of adiabatic density perturbations. However ΛCDM itself offers no explanation

for how these conditions occurred. The theory of inflation is an extension to the standard model, which postulates a phase of exponential expansion at a still earlier epoch ($\sim 10^{-35}$ s) that precedes ΛCDM and produces the required initial conditions (See Ref. [3] for a recent review and citations to the original literature.)

There is widespread support for the claim that existing observations already indicate that some version of inflation probably did occur, but there are also skeptics. However there is an additional relic which inflation predicts, and which one can attempt to detect. Inflation launches tensor mode perturbations into the fabric of space-time which will propagate unimpeded as inflationary gravitational waves (IGWs) down to the present day. Their amplitude is diminished with the expansion of the Universe, and detection at the present epoch is not feasible with current technology. The most promising potential method of detection is to look for their signature written into the pattern of the CMB at last scattering, 380,000 years after the beginning. Inflationary theories generically predict that IGWs exist, but many specific models have been proposed producing a wide range of amplitudes—with some being unobservably small. The size of the IGW signal is conventionally expressed as the initial ratio of the tensor and scalar perturbation amplitudes r.

In the ΛCDM standard model the CMB is polarized by Thomson scattering of Doppler induced quadrupoles in the local radiation field at last scattering, arising from flows sourced by density perturbations. This naturally produces a polarization pattern with direction parallel/perpendicular to the gradient of its intensity—this is curl-free, or E-mode polarization, and was first detected in Ref. [4]. Due to small gravitational deflections of the CMB photons in flight by intervening large scale structure the initial purity of the E-mode pattern is disturbed and a small lensing B-mode is produced at sub-degree angular scales.

IGWs are intrinsically quadrupolar distortions of the metric and produce both E and B-mode polarization depending on their orientation with respect to our last scattering surface. However, due to the large ΛCDM E-mode signal, the most promising place to search for an IGW signal is in B-modes. Furthermore, since the IGW B-modes have a much redder spectrum than the lensing B-modes, the best place to look is at angular scales larger than a few degrees (multipoles $\ell < 100$). Limits on IGW from non-polarized CMB observations are now fully saturated at cosmic variance limits [2] and it is generally agreed that the best (only) way to make further progress is through improved measurements of CMB B-modes.

The BICEP and *Keck Array* telescopes are small aperture polarimeters specifically designed to search for an IGW signal at the recombination bump ($\ell \approx 80$). BICEP1 operated from 2006 to 2008 and set a limit $r < 0.70$ at 95% confidence [5]. BICEP2 operated from 2010 to 2012 at 150 GHz and in Ref. [6] reported a detection of a substantial excess over the lensed-ΛCDM expectation in the multipole range $30 < \ell < 150$. Additional measurements at 150 GHz taken by the *Keck Array* during 2012 and 2013 confirmed this excess [7]. However, new data from the *Planck* space mission provided evidence that emission from galactic dust grains could be more polarized at high galactic latitudes than anticipated [8, 9], a possibility emphasized by [10, 11]. Analysis of the combined BICEP2 and *Keck Array* 150 GHz data in combination with data from *Planck* (principally at 353 GHz) showed that a substantial part of the 150 GHz excess is due to polarized emission from galactic dust grains, and that once this is accounted for, the result becomes $r_{0.05} < 0.12$ at 95% confidence [12].

BICEP2 was a simple 26 cm aperture all-cold refractor, and *Keck Array* is basically five copies of this on a single telescope mount [7, 13]. Both are sited at the South Pole in Antarctica, taking advantage of the dry atmosphere and stable observing conditions. In addition to the all-cold optics these telescopes have two features which aid greatly in the suppression and characterization of instrumental systematics: i) they are equipped with co-moving absorptive forebaffles resulting in extremely low far side-lobe response, and ii) the entire instrument can be rotated about the line of sight allowing modulation of polarized signal.

Keck Array was designed at the outset to observe in multiple frequency bands—the 2012 and 2013 observations were all taken at 150 GHz because detectors for other bands were not yet ready. Before the 2014 season two of the five receivers of *Keck Array* were refitted for operation in a band centered on 95 GHz (the other three receivers remaining at 150 GHz). In this paper we fold in this new data and perform a multi-component, multi-spectral likelihood analysis similar to our previous analysis [12].

This paper builds on the initial BICEP2 results paper [6, hereafter BK-I], the *Keck* 2012+2013 results paper [7, hereafter BK-V], and the BICEP2/*Keck*/*Planck* analysis paper [12, hereafter BKP].

Instrument and observations.—The *Keck Array* instrument is described in Sec. 2 of BK-V. (See also the BICEP2 Instrument Paper [13] for further details.) Before the 2014 observing season two of the receivers of *Keck Array* were removed, the lenses and filters were replaced with versions optimized for a band centered at 95 GHz, and the focal planes were replaced with units loaded with appropriately scaled versions of our antenna-coupled detectors [14]. Because the physical size of these antennas is larger each of the four tiles contains only a 6×6 array (rather than 8×8 at 150 GHz). With two focal planes at 95 GHz this gives 288 total detector pairs (576 total detectors). The 150 GHz receivers remained unchanged from the 2013 season.

During the 2014 austral winter season the array was operated exactly as for the previous seasons. A $\sim 1\%$ region of sky centered at RA 0h, Dec. $-57.5°$ was observed from March until November over ≈ 4600 fifty minute "scansets". Efficiency and yield was similar to previous

seasons. See Sec. 4 of BK-V for further details of the observing strategy and data selection.

BICEP2/Keck Maps.—The processing from time stream to maps is identical to that described in Sec. III & IV of BK-I and summarized in Sec. 5 of BK-V. Relative gain calibration is applied between the two halves of each pair and the difference is taken. Filtering is then applied to remove residual atmospheric noise and any ground-fixed (scan-synchronous) pickup. The data are then binned into simple map pixels and, with knowledge of the polarization sensitivity directions, maps of Stokes parameters Q and U are formed. "Deprojection" is also performed to remove leakage of temperature to polarization due to beam systematics and this results in an additional filtering of signal.

Fig. 1 shows the 95 & 150 GHz Q/U maps combining data from BICEP2 (2010–2012) and *Keck Array* (2012–2014)—we refer to these as the BK14 maps meaning that they contain all data up to and including that taken during the 2014 observing season. The 150 GHz maps add 3 more receiver years to the previous 13 in the BK13 based analysis of BKP, and modestly improves the Q/U sensitivity from 57 nK deg to 50 nK deg (3.0 μK arcmin) over an effective area of 395 square degrees. These are the deepest maps of CMB polarization published to date. The 95 GHz maps contain only 2 receiver years of data and the Q/U sensitivity is 127 nK deg (7.6 μK arcmin) over an effective area of 375 square degrees. (The survey weight is thus 310,000 (47,000) μK^{-2} at 150 (95) GHz.) The 95 GHz beam is wider (43 arcmin versus 30 arcmin FWHM) and we see the effect of the additional beam smoothing. However the degree scale structure is clearly near identical at both frequencies. While there is a dust component hidden in the 150 GHz maps it is highly subdominant to ΛCDM E-mode signal. See Appendix A for the full set of $T/Q/U$ signal and noise maps.

External Maps.—We use the Public Release 2 "full mission" maps available from the *Planck* Legacy Archive [15][16], noting that these are near identical to those used in BKP. For this analysis we also add the WMAP9 23 GHz (K-band) and 33 GHz (Ka-band) maps [17][18].

For each of these external maps we deconvolve the native instrument beam, reconvolve the Keck 150 GHz beam, and then process the result through an "observing" matrix to produce a map with the same filtering of spatial modes as the 150 GHz map. See Sec. II.A of BKP for further details of this process. For *Planck* we use the FFP8 simulations [19] and for WMAP we use simple inhomogeneous white noise simulations derived from the provided variance maps.

Power Spectra.—We convert the maps to power spectra using the methods described in Sec. VI of BK-I including the matrix based purification operation to prevent E to B mixing. We generate separate purification matrices to match the filtering of the 95 & 150 GHz maps.

We first subject the new 95 GHz data to our usual suite of "jackknife" internal consistency checks. The re-

sults are given in Appendix B and show empirically that the data are free of systematic contamination at a level greater than the noise. In addition in Appendix C we investigate the stability of the previous 150 GHz spectrum when adding the new 2014 data—there is no indication of problems.

We now proceed to comparing the spectra and cross spectra of our 95 and 150 GHz maps—Fig. 2 shows the results. We use a common apodization mask as the geometric mean of the two (smoothed) inverse variance maps. The EE spectra agree to within much better than the nominal errorbar size because the uncertainty is dominated by sample variance and we are observing the same piece of sky. To make a rough estimate of the significance of deviation from lensed-ΛCDM, we calculate χ^2 and χ (sum of normalized deviations) as shown on the plot. We see strong evidence for excess BB power in BK14$_{150}$×BK14$_{150}$ and moderate evidence in BK14$_{95}$×BK14$_{150}$. Dashed lines for the lensed-ΛCDM+dust model derived in BKP are over-plotted and appear to be consistent with the new data.

Fig. 3 shows selected BB cross spectra between the BK14 95 & 150 GHz maps and the *Planck* (P) and WMAP (W) bands. There is no strong evidence for detection of synchrotron emission—W$_{23}$×BK14$_{95}$ and W$_{23}$×BK14$_{150}$ are both mildly elevated but P$_{30}$×BK14$_{150}$ has stronger nominal anticorrelation (as noted in the BKP paper). W$_{33}$×BK14$_{95}$ and W$_{33}$×BK14$_{150}$ are both consistent with null. The only strong detections of excess signal are in BK14$_{150}$×P$_{353}$ and, at lower significance BK14$_{150}$×P$_{217}$. See Appendix D for the full set of auto- and cross-spectra.

Likelihood Analysis.—We next proceed to a multicomponent, multi-spectral likelihood analysis which is an expanded version of that described in Sec. III of the BKP paper. We compute the likelihood of the data for any given proposed model using an extended version of the HL approximation [20] and the full covariance matrix of the auto- and cross-spectral bandpowers as derived from simulations (setting to zero terms whose expectation value is zero).

In this analysis we primarily use a lensed-ΛCDM+dust+synchrotron+r model and explore the parameter space using COSMOMC [21]. The COSMOMC module containing the data and model is available for download at http://bicepkeck.org. In this paper the "baseline" analysis is defined to:

- Use the BK14 maps as shown in Figure 1 (all BICEP2/*Keck* data up to and including that taken during the 2014 observing season).

- Use all the polarized bands of *Planck* (30–353 GHz) plus the 23 & 33 GHz bands of WMAP.

- Use all possible BB auto- and cross-spectra between these maps. This includes all the spectra shown in Figures 2 & 3 plus many more. Spectra with no detection can of course still have constraining power—for instance non-detection in P$_{30}$×P$_{353}$
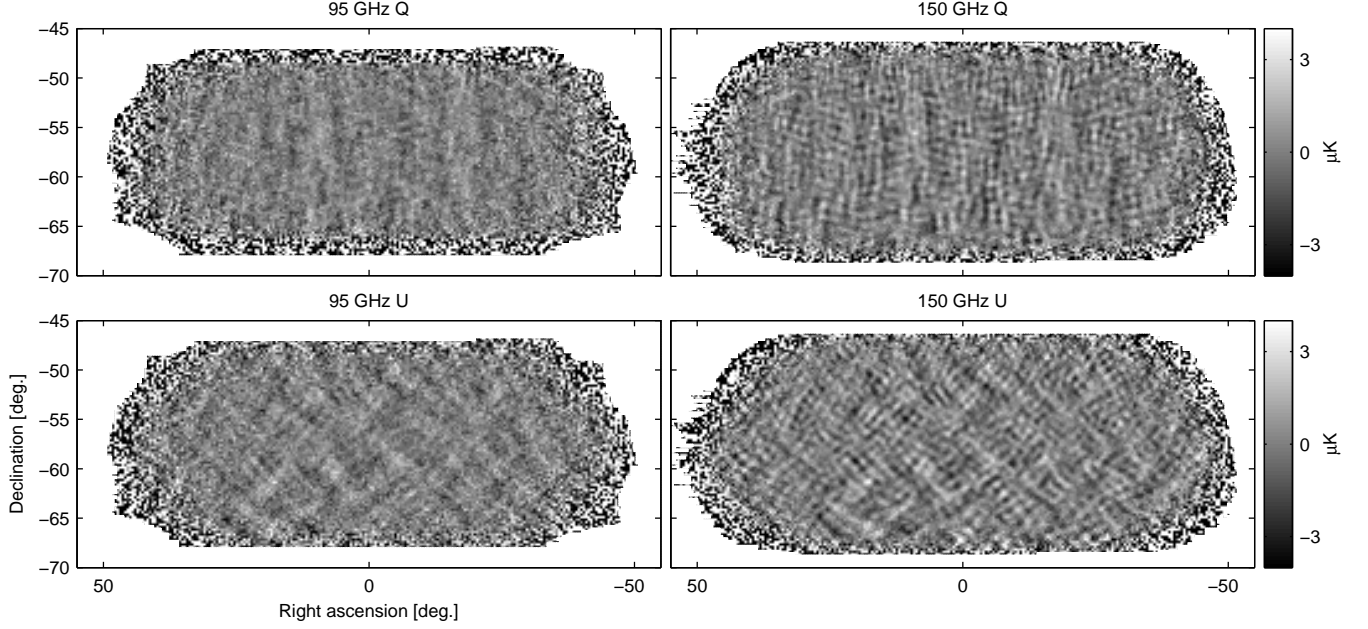
FIG. 1. Deep Q/U maps at 95 & 150 GHz using all BICEP2/*Keck* data through the end of the 2014 observing season—we refer to these maps as BK14. Noise levels are 127 nK deg (left) and 50 nK deg (right). All maps show a high signal-to-noise pattern dominated by E-mode polarization; the 95 GHz maps appear smoother because of the larger beam size.
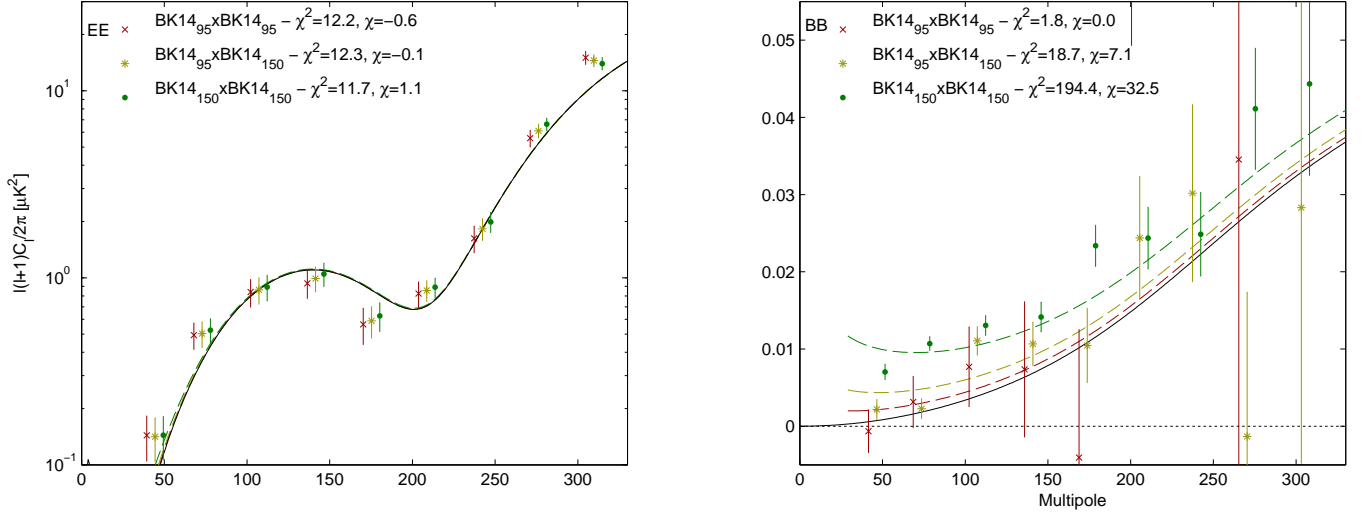

FIG. 2. *EE* and *BB* auto- and cross-spectra between 95 & 150 GHz using all BICEP2/*Keck* data up to and including that taken during the 2014 observing season—we refer to these spectra as BK14. (For clarity the sets of points are offset horizontally.) The solid black curves show the lensed-ΛCDM theory spectra. The error bars are the standard deviations of the lensed-ΛCDM+noise simulations and hence contain no sample variance on any additional signal component. The χ^2 and χ (sum of deviations) against lensed-ΛCDM for the lowest five bandpowers are given, and can be compared to their expectation value/standard-deviation of 5/3.1 and 0/2.2 respectively The dashed lines show a lensed-ΛCDM+dust model derived from our previous analysis.

disfavors sync/dust correlation. (The complete set are shown in Appendix D.)

- Use nine bandpowers spanning the range $20 < \ell < 330$.

- Include dust with amplitude $A_{d,353}$ evaluated at 353 GHz and $\ell = 80$. As in the BKP analysis the frequency spectral behavior is taken as a simple modified black body spectrum with $T_d = 19.6$ K and $\beta_d = 1.59 \pm 0.11$, using a Gaussian prior with
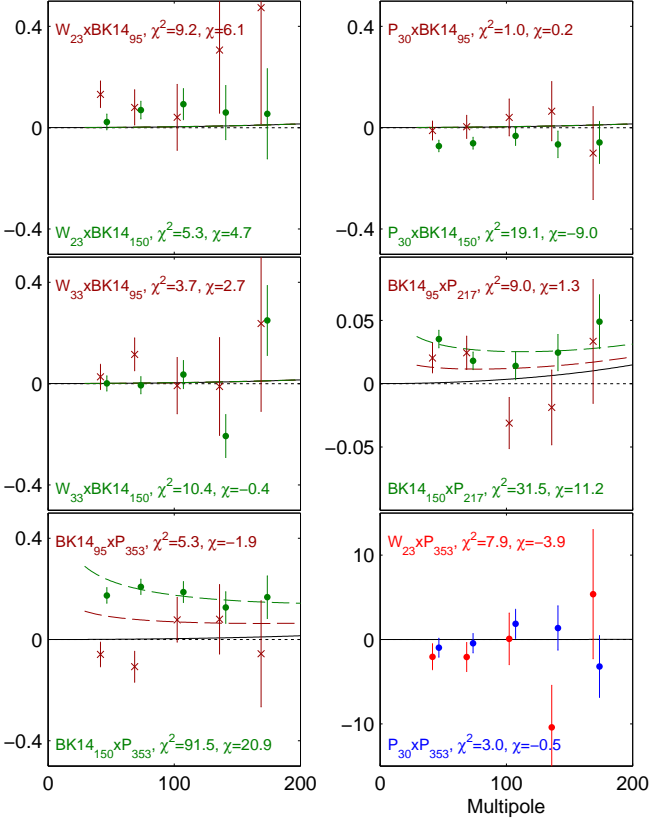
FIG. 3. Selected BB cross-spectra between the BK14 maps at 95 (red) & 150 GHz (green) and the external maps of WMAP and *Planck*. The quantity plotted is $\ell(\ell+1)C_l/2\pi$ (μK^2), and the error bars are the standard deviations of the lensed-ΛCDM+noise simulations. The solid black curves show the lensed-ΛCDM theory spectrum and the χ^2 and χ versus this model are shown. $W_{23}\times BK14_{95}$ and $W_{23}\times BK14_{150}$ are both mildly elevated showing weak evidence for synchrotron but $P_{30}\times BK14_{150}$ has stronger nominal anticorrelation. We see modest evidence for detection of dust emission in $BK14_{150}\times P_{217}$ and strong evidence in $BK14_{150}\times P_{353}$. The dashed lines show a lensed-ΛCDM+dust model derived from our previous analysis.

the given 1σ width. (Analyzing polarized emission at intermediate galactic latitudes Fig. 11 of Ref. [22] shows that this model is accurate in the mean to within a few percent over the frequency range 100–353 GHz, while the patch-to-patch fluctuation is noise dominated.) The spatial power spectrum is taken as a simple power law $\mathcal{D}_\ell \propto \ell^{\alpha_d}$ marginalizing over the range $-1 < \alpha_d < 0$. (Where $\mathcal{D}_\ell \equiv \ell(\ell+1)C_l/2\pi$.)

- Include synchrotron with amplitude $A_{sync,23}$ evaluated at 23 GHz and $\ell = 80$, assuming a simple power law for the frequency spectral behavior $A_{sync} \propto \nu^{\beta_s}$ with a Gaussian prior $\beta_s = -3.1 \pm 0.3$ [23]. The spatial power spectrum is taken as a simple power law $\mathcal{D}_\ell \propto \ell^{\alpha_s}$ marginalizing over the

range $-1 < \alpha_s < 0$.

- Allow sync/dust correlation and marginalize over the correlation parameter $0 < \epsilon < 1$.

- Quote the tensor/scalar power ratio r at a pivot scale of 0.05 Mpc^{-1} and fix the tensor spectral index $n_t = 0$.

See Appendix E 1 for a more detailed explanation of these choices.

Results of this baseline analysis are shown in Fig. 4 and yield the following statistics: $r_{0.05} = 0.028^{+0.026}_{-0.025}$, $r_{0.05} < 0.090$ at 95% confidence, $A_{d,353} = 4.3^{+1.2}_{-1.0}\,\mu K^2$, and $A_{sync,23} < 3.8\,\mu K^2$ at 95% confidence. For r the zero-to-peak likelihood ratio is 0.63. Taking $\frac{1}{2}(1 - f(-2\log L_0/L_{peak}))$, where f is the χ^2 cdf (for one degree of freedom), we estimate that the probability to get a likelihood ratio smaller than this is 18% if in fact $r = 0$. Running the analysis on the lensed-ΛCDM+dust+noise simulations produces a similar number. The zero-to-peak likelihood ratio for A_d indicates that the detection of dust is now $> 8\sigma$.

Results for the additional parameters are shown in the upper right part of Fig. 4. The dust frequency spectral parameter β_d pulls weakly against the prior to higher values. The synchrotron frequency spectral parameter β_s just reflects the prior (as expected since synchrotron is not strongly detected). The data have a mild preference for values of α_d close to the -0.42 found in Ref. [9], while α_s is unconstrained. The data disfavor strong sync/dust correlation (due to the non detection of signal in spectra like $W_{23}\times P_{353}$—see Fig 3). As A_{sync} approaches zero ϵ becomes unconstrained leading to an increase in the available parameter volume, and the "flare" in the A_{sync} constraints.

The maximum likelihood model (including priors) has parameters $r = 0.026$, $A_{d,353} = 4.1\,\mu K^2$, $A_{sync,23} = 1.4\,\mu K^2$, $\beta_d = 1.6$, $\beta_s = -3.1$, $\alpha_d = -0.19$, $\alpha_s = -0.56$, and $\epsilon = 0.00$. This model appears to be an acceptable fit to the data—see Appendix D for further details.

In Figure 4 we see that as compared to the primary BKP analysis the peak position of the likelihood curve for r has shifted down slightly. In Figure 5 we investigate why. Although we have made extensive changes to the model these make only a small difference. (See Appendix E 1 for details of these changes.) The change from the BK13$_{150}$ to the BK14$_{150}$ maps causes some of the downward shift in the peak position. This may seem surprising given that only a relatively small amount of additional data has been added ($\sim 20\%$). However Appendix C shows that the shifts in the bandpower values are not unlikely and we should therefore accept the shift in the r constraint as simply due to noise fluctuation. Adding in the BK14$_{95}$ data produces an additional downward shift in the peak position, and also significantly narrows the likelihood curve.

Figure 5 shows one additional variation. It turns out that the tight prior on β_d from *Planck* analysis of other
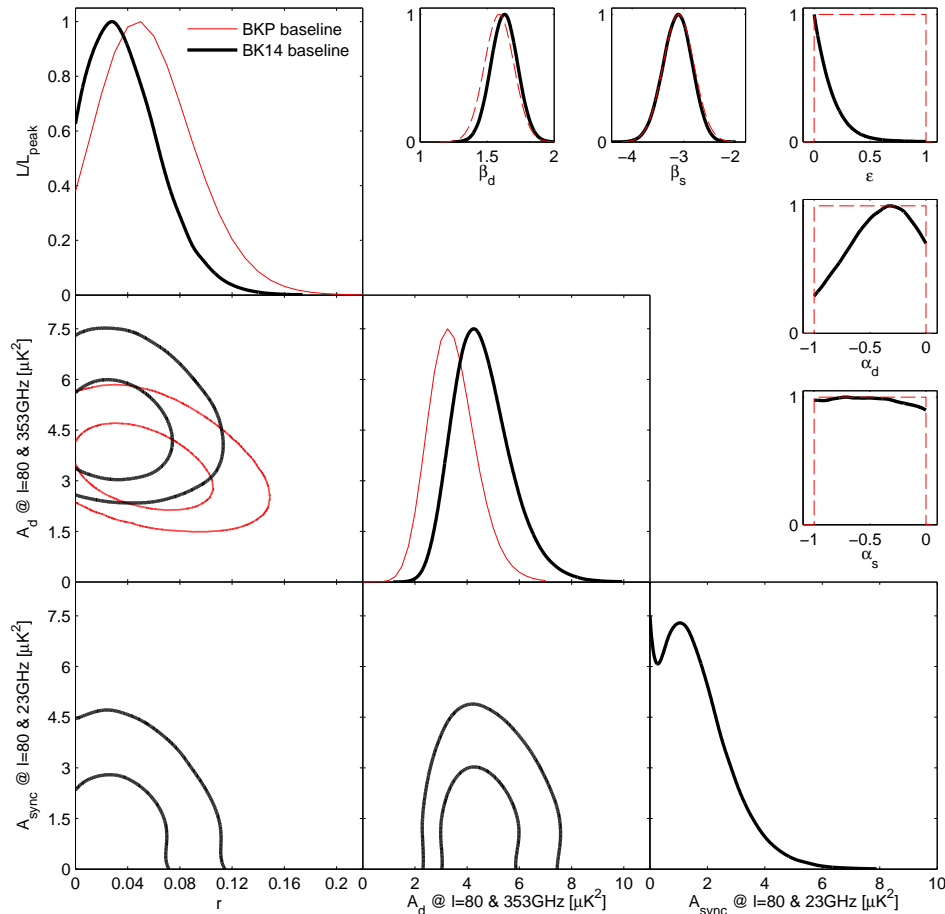
FIG. 4. Results of a multicomponent multi-spectral likelihood analysis of BICEP2/*Keck*+external data. The red faint curves are the primary result from the previous BKP paper (the black curves from Fig. 6 of that paper). The bold black curves are the new baseline BK14 results. Differences between these analyses include adding synchrotron to the model, including additional external frequency bands from WMAP & *Planck*, and adding *Keck Array* data taken during the 2014 observing season at 95 & 150 GHz. We see that the peak position of the tensor/scalar ratio curve r shifts down slightly and the upper limit tightens to $r_{0.05} < 0.09$ at 95% confidence. The parameters A_d and A_sync are the amplitudes of the dust and synchrotron B-mode power spectra, where β and α are the respective frequency and spatial spectral indices. The correlation coefficient between the dust and synchrotron patterns is ϵ. In the β, α and ϵ panels the dashed red lines show the priors placed on these parameters (either Gaussian or uniform).

regions of sky is becoming unnecessary. Removing the prior the peak position of the likelihood on r shifts up slightly and broadens so that $r = 0.043^{+0.033}_{-0.031}$ & $r < 0.11$ (95%), while the likelihood curve for β_d is close to Gaussian in shape with mean/σ of 1.82/0.26. In Appendix E 2 we investigate a variety of other variations from the baseline analysis and in Appendix E 3 we perform some validation tests of the likelihood using simulations.

For the purposes of presentation we also run a likelihood analysis to find the CMB and foreground contributions on a bandpower-by-bandpower basis. The baseline analysis is a single fit to all 9 bandpowers across 66 spectra with 8 parameters. Instead we now perform 9 separate fits—one for each bandpower—across the 66 spectra, with 6 parameters in each fit. These 6 parameters are the amplitudes of CMB, dust and synchrotron

plus β_d, β_s, and ϵ with identical priors to the baseline analysis. The results are shown in Fig. 6—the resulting CMB bandpowers are consistent with lensed-ΛCDM while the dust bandpowers are consistent with the level of dust found in the baseline analysis. Synchrotron is tightly limited in all the bandpowers.

Conclusions.—As shown above, the BK14 data in combination with external maps produce B-mode based constraints on the tensor-to-scalar ratio r which place an upper limit $r_{0.05} < 0.09$ at 95% confidence. The analysis of *Planck* full mission TT data in conjunction with external data produces the constraint $r_{0.002} < 0.11$ ($r_{0.05} < 0.12$) at 95% confidence ("*Planck* TT+lowP+lensing+ext" in Equation 39b of Ref. [2]), and are saturated at cosmic variance limits. The BK14 result constitutes the first B-mode constraints that clearly surpass those from tem-
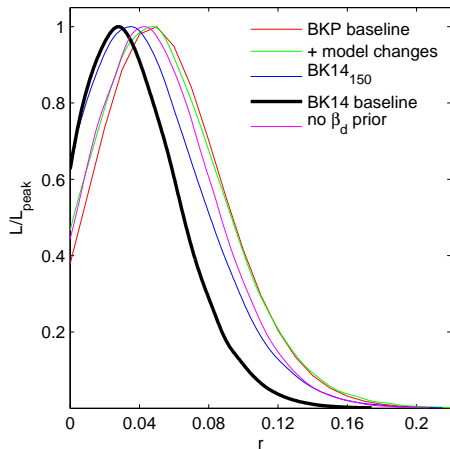
FIG. 5. Likelihood results on r for several intermediate steps between the BKP (previous) and BK14 (current) analyses. See text for details.
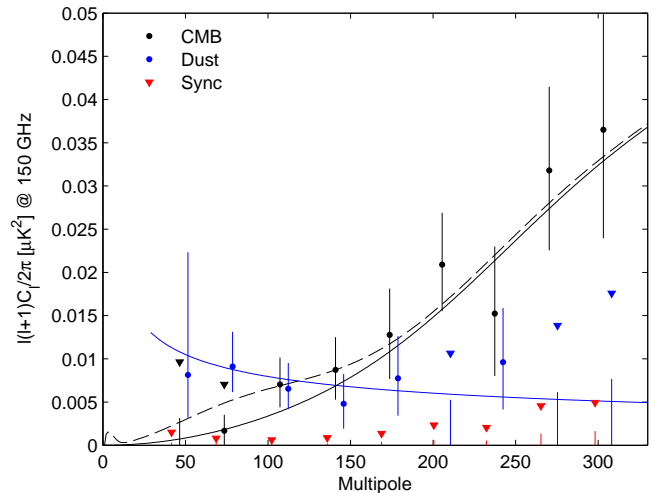

FIG. 6. Spectral decomposition of the BB data into synchrotron (red), CMB (black) and dust (blue) components. The decomposition is calculated independently in each bandpower, marginalizing over β_d, β_s, and ϵ with the same priors as the baseline analysis. Error bars denote 68% credible intervals, with the point marking the most probable value. If the 68% interval includes zero, we also indicate the 95% upper limit with a downward triangle. (For clarity the sets of points are offset horizontally.) The solid black line shows lensed-ΛCDM with the dashed line adding on top an $r = 0.05$ tensor contribution. The blue curve shows a dust model consistent with the baseline analysis ($A_{d,353} = 4.3\,\mu K^2$, $\beta_d = 1.6$, $\alpha_d = -0.4$).

perature anisotropies. In Fig. 7 we reproduce Ref. [2]'s result in the r vs. n_s plane, and show the effect of adding in our BK14 B-mode data. The allowed region tightens and the joint result is $r_{0.05} < 0.07$ (95%), although as emphasized in Ref. [2] the TT derived constraints on r are more model dependent than BB ones.

Fig. 8 compares signal levels and current noise uncertainties in the critical $\ell \sim 80$ bandpower (updated from Fig. 13 of BKP). A second season of 95 GHz *Keck Array* data has already been recorded (in 2015) and will push the 95×95 point down by factor 2. During 2015 two receivers were also operated in a third band centered on 220 GHz, producing deep maps which will improve dust separation. This 2015 data is under analysis and will be reported on in a future paper. In addition, BICEP3 began operations in 2015 in the 95 GHz band.

In this paper, we have presented an analysis of all BICEP2/*Keck* data up through the 2014 season, adding, for the first time, 95 GHz data from the *Keck Array*. We have updated our multi-frequency likelihood analysis with a more extensive foreground parameterization and the inclusion of external data from the 23 & 33 GHz bands of WMAP, in addition to all seven polarized bands of *Planck*. The baseline analysis yields $r_{0.05} = 0.028^{+0.026}_{-0.025}$ and $r_{0.05} < 0.09$ at 95% confidence, constraints that are robust to the variations explored in analysis and priors. With this result, B-modes now offer the most powerful limits on inflationary gravitational waves, surpassing constraints from temperature anisotropies and other evidence for the first time. With upcoming multifrequency data the B-mode constraints can be expected to steadily improve.

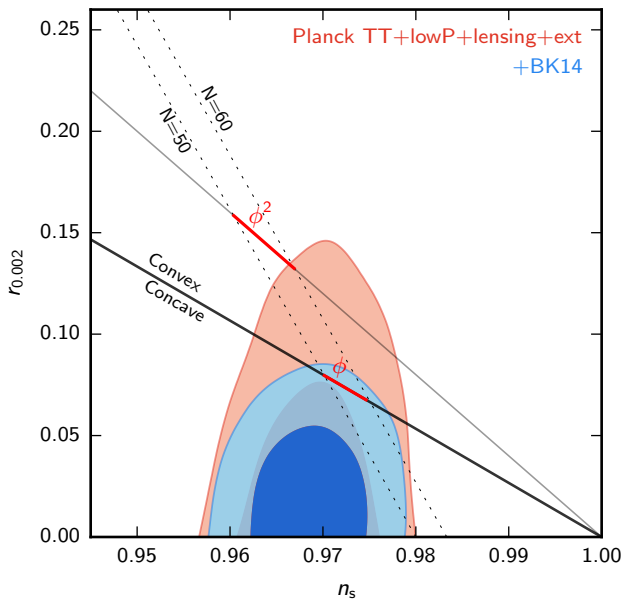also thank the *Planck* and WMAP teams for the use of their data.

FIG. 7. Constraints in the r vs. n_s plane when using *Planck* plus additional data, and when also adding BICEP2/*Keck* data through the end of the 2014 season including new 95 GHz maps—the constraint on r tightens from $r_{0.05} < 0.12$ to $r_{0.05} < 0.07$. This figure is adapted from Fig. 21 of Ref. [2]— see there for further details.

* jmkovac@cfa.harvard.edu
† pryke@physics.umn.edu

[1] A. A. Penzias and R. W. Wilson, Astrophys. J. **142**, 419 (1965).

[2] Planck Collaboration 2015 XIII, ArXiv e-prints (2015), arXiv:1502.01589.

[3] M. Kamionkowski and E. D. Kovetz, ArXiv e-prints (2015), arXiv:1510.06042.

[4] J. M. Kovac, E. M. Leitch, C. Pryke, J. E. Carlstrom, N. W. Halverson, and W. L. Holzapfel, Nature (London) **420**, 772 (2002).

[5] BICEP1 Collaboration, Astrophys. J. **783**, 67 (2014), arXiv:1310.1422.

[6] BICEP2 Collaboration I, Phys. Rev. Lett. **112**, 241101 (2014).

[7] *Keck Array* and BICEP2 Collaborations V, Astrophys. J. **811**, 126 (2015), arXiv:1502.00643.

[8] Planck Collaboration Int. XIX, Astron. Astrophys. **576**, A104 (2015), arXiv:1405.0871.

[9] Planck Collaboration Int. XXX, ArXiv e-prints (2014), arXiv:1409.5738.

[10] R. Flauger, J. C. Hill, and D. N. Spergel, J. Cosmol. Astropart. Phys. **8**, 039 (2014), arXiv:1405.7351.

[11] M. J. Mortonson and U. Seljak, J. Cosmol. Astropart. Phys. **10**, 035 (2014), arXiv:1405.5857.

[12] BICEP2/*Keck* and *Planck* Collaborations, Physical Review Letters **114**, 101301 (2015), arXiv:1502.00612.

[13] BICEP2 Collaboration II, Astrophys. J. **792**, 62 (2014).

[14] BICEP2/*Keck* and Spider Collaborations, Astrophys. J. **812**, 176 (2015), arXiv:1502.00619 [astro-ph.IM].

[15] See http://www.cosmos.esa.int/web/planck/pla.

[16] Planck Collaboration 2015 I, ArXiv e-prints (2015), arXiv:1502.01582.

[17] See http://lambda.gsfc.nasa.gov/product/map/dr5/m_products.cfm.

[18] C. L. Bennett, D. Larson, J. L. Weiland, N. Jarosik, G. Hinshaw, N. Odegard, K. M. Smith, R. S. Hill, B. Gold, M. Halpern, E. Komatsu, M. R. Nolta, L. Page, D. N. Spergel, E. Wollack, J. Dunkley, A. Kogut, M. Limon, S. S. Meyer, G. S. Tucker, and E. L. Wright, Astrophys. J. Suppl. Ser. **208**, 20 (2013), arXiv:1212.5225.

[19] Planck Collaboration 2015 XII, ArXiv e-prints (2015), arXiv:1509.06348.

[20] S. Hamimeche and A. Lewis, Phys. Rev. D **77**, 103013 (2008), arXiv:0801.0554.

[21] A. Lewis and S. Bridle, Phys. Rev. **D66**, 103511 (2002), astro-ph/0205436.

[22] Planck Collaboration Int. XXII, Astron. Astrophys. (2014), arXiv:1405.0874.

[23] U. Fuskeland, I. K. Wehus, H. K. Eriksen, and S. K. Næss, Astrophys. J. **790**, 104 (2014), arXiv:1404.5323.

[24] See http://lambda.gsfc.nasa.gov/product/map/dr5/mcmc_maps_info.cfm.

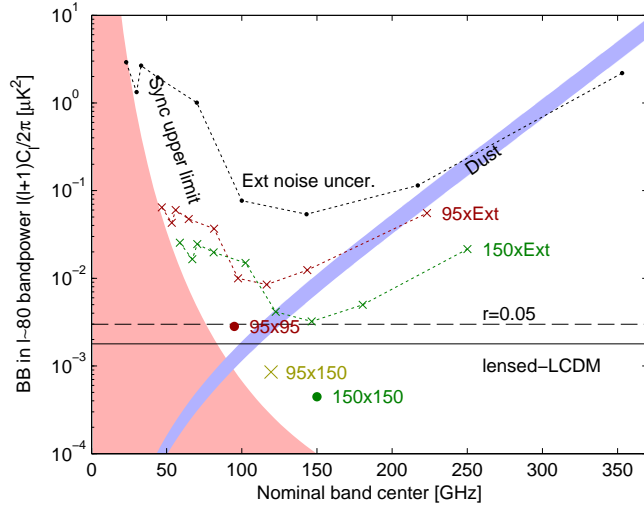[25] S. K. Choi and L. A. Page, ArXiv e-prints (2015), arXiv:1509.05934.

FIG. 8. Expectation values and noise uncertainties for the $\ell \sim 80$ BB bandpower in the BICEP2/*Keck* field. The solid and dashed black lines show the expected signal power of lensed-ΛCDM and $r = 0.05$. Since CMB units are used, the levels corresponding to these are flat with frequency. The blue band shows a dust model consistent with the baseline analysis ($A_{\mathrm{d},353} = 4.3^{+1.2}_{-1.0}\,\mu\mathrm{K}^2$, $\beta_d = 1.6$) while the pink shaded region shows the allowed region for synchrotron ($A_{\mathrm{sync},23} < 3.8\,\mu\mathrm{K}^2$, $\beta_{\mathrm{s}} = -3.1$). The BICEP2/*Keck* noise uncertainties are shown as large colored symbols, and the noise uncertainties of the WMAP/*Planck* single-frequency spectra evaluated in the BICEP2/*Keck* field are shown in black. The red (green) crosses show the noise uncertainty of the cross-spectra taken between 95 (150) GHz and, from left to right, 23, 30, 33, 44, 70, 100, 143, 217 & 353 GHz, and are plotted at horizontal positions such that they can be compared vertically with the dust and sync curves.

[26] J. Dunkley, A. Amblard, C. Baccigalupi, M. Betoule, D. Chuss, A. Cooray, J. Delabrouille, C. Dickinson, G. Dobler, J. Dotson, H. K. Eriksen, D. Finkbeiner, D. Fixsen, P. Fosalba, A. Fraisse, C. Hirata, A. Kogut, J. Kristiansen, C. Lawrence, A. M. Magalhães, M. A. Miville-Deschenes, *et al.*, AIP Conf. Proc. **1141**, 222 (2009), arXiv:0811.3915.

Appendix A: Maps

Figures 9 & 10 show the full sets of $T/Q/U$ maps at 150 & 95 GHz. The right side of each figure shows realizations of noise created by randomly flipping the sign of data subsets while coadding the map—see Sec. V.B of BK-I for further details.

Appendix B: *Keck Array* 95 GHz Power Spectra and Internal Consistency Tests

A powerful internal consistency test are data split difference tests which we refer to as "jackknifes". As well as the full coadd signal maps we also form many pairs of split maps where the splits are chosen such that one might expect different systematic contamination in the two halves of the split. The split halves are differenced and the power spectra taken. We then take the deviations of these from the mean of signal+noise simulations and form χ^2 and χ (sum of deviations) statistics. In this section we perform tests of the new 95 GHz data set which are exactly analogous to the tests of the previous 150 GHz data sets performed in Sec. VII.C of BK-I and Sec. 6.3 of BK-V. Fig. 11 shows the signal spectra and a sample set of jackknife spectra. All the signal spectra are consistent with lensed-ΛCDM and the jackknife spectra with null.

Table I shows the χ^2 and χ statistics for the full set of 95 GHz jackknife tests and Fig. 12 presents the same results in graphical form. Note that these values are partially correlated—particularly the 1–5 and 1–9 versions of each statistic. We conclude that there is no evidence for corruption of the data at a level exceeding the noise.

Appendix C: 150 GHz Spectral Stability

Questions were raised as to whether the BICEP2 and *Keck Array* 2012+2013 BB spectra are mutually compatible. We investigated this in Sec. 8 of BK-V and concluded that they are. Here we perform a similar test on the difference of the BK13$_{150}$ and BK14$_{150}$ spectra—i.e. when adding the additional 150 GHz data from 2014. We compare the differences of the real spectra to the differences of simulations which share the same underlying input skies. Fig. 13 shows the results. While the bandpowers do shift around even when adding only $\sim 20\%$ of additional data these shifts are seen to be consistent with noise fluctuation.

Appendix D: Additional Spectra

Figures 2 & 3 show only a small subset of the spectra which are used in the likelihood analysis and included in the `COSMOMC` input file. We are using two BICEP2/*Keck* bands, two WMAP bands, and seven

TABLE I. Jackknife PTE values from χ^2 and χ (sum of deviations) tests for *Keck Array* 95 GHz data taken in 2014. This table is analogous to Table I of BK-I and Table 4 of BK-V.

| Jackknife	Band powers 1–5 χ^2	Band powers 1–9 χ^2	Band powers 1–5 χ	Band powers 1–9 χ
Deck jackknife				
EE	0.625	0.591	0.523	0.569
BB	0.166	0.192	0.076	0.020
EB	0.876	0.539	0.814	0.445
Scan Dir jackknife				
EE	0.439	0.513	0.760	0.423
BB	0.944	0.535	0.565	0.168
EB	0.539	0.192	0.912	0.980
Tag Split jackknife				
EE	0.543	0.537	0.810	0.938
BB	0.768	0.780	0.687	0.539
EB	0.313	0.547	0.407	0.451
Tile jackknife				
EE	0.234	0.477	0.395	0.709
BB	0.050	0.072	0.012	0.046
EB	0.828	0.902	0.812	0.822
Phase jackknife				
EE	0.862	0.982	0.577	0.471
BB	0.944	0.521	0.639	0.325
EB	0.691	0.890	0.204	0.357
Mux Col jackknife				
EE	0.084	0.146	0.182	0.337
BB	0.172	0.337	0.012	0.152
EB	0.541	0.695	0.956	0.812
Alt Deck jackknife				
EE	0.098	0.076	0.030	0.036
BB	0.092	0.126	0.102	0.140
EB	0.858	0.842	0.858	0.741
Mux Row jackknife				
EE	0.232	0.289	0.699	0.918
BB	0.289	0.267	0.082	0.014
EB	0.148	0.130	0.996	0.998
Tile/Deck jackknife				
EE	0.924	0.956	0.162	0.399
BB	0.507	0.034	0.561	0.343
EB	0.477	0.361	0.954	0.994
Focal Plane inner/outer jackknife				
EE	0.477	0.335	0.200	0.792
BB	0.886	0.437	0.762	0.569
EB	0.595	0.876	0.926	0.780
Tile top/bottom jackknife				
EE	0.261	0.519	0.998	0.990
BB	0.756	0.890	0.415	0.431
EB	0.850	0.920	0.377	0.317
Tile inner/outer jackknife				
EE	0.184	0.353	0.427	0.529
BB	0.772	0.772	0.749	0.707
EB	0.407	0.038	0.934	0.667
Moon jackknife				
EE	0.569	0.701	0.228	0.251
BB	0.305	0.465	0.978	0.990
EB	0.349	0.507	0.677	0.301
A/B offset best/worst				
EE	0.635	0.267	0.104	0.431
BB	0.407	0.387	0.677	0.287
EB	0.321	0.605	0.860	0.685
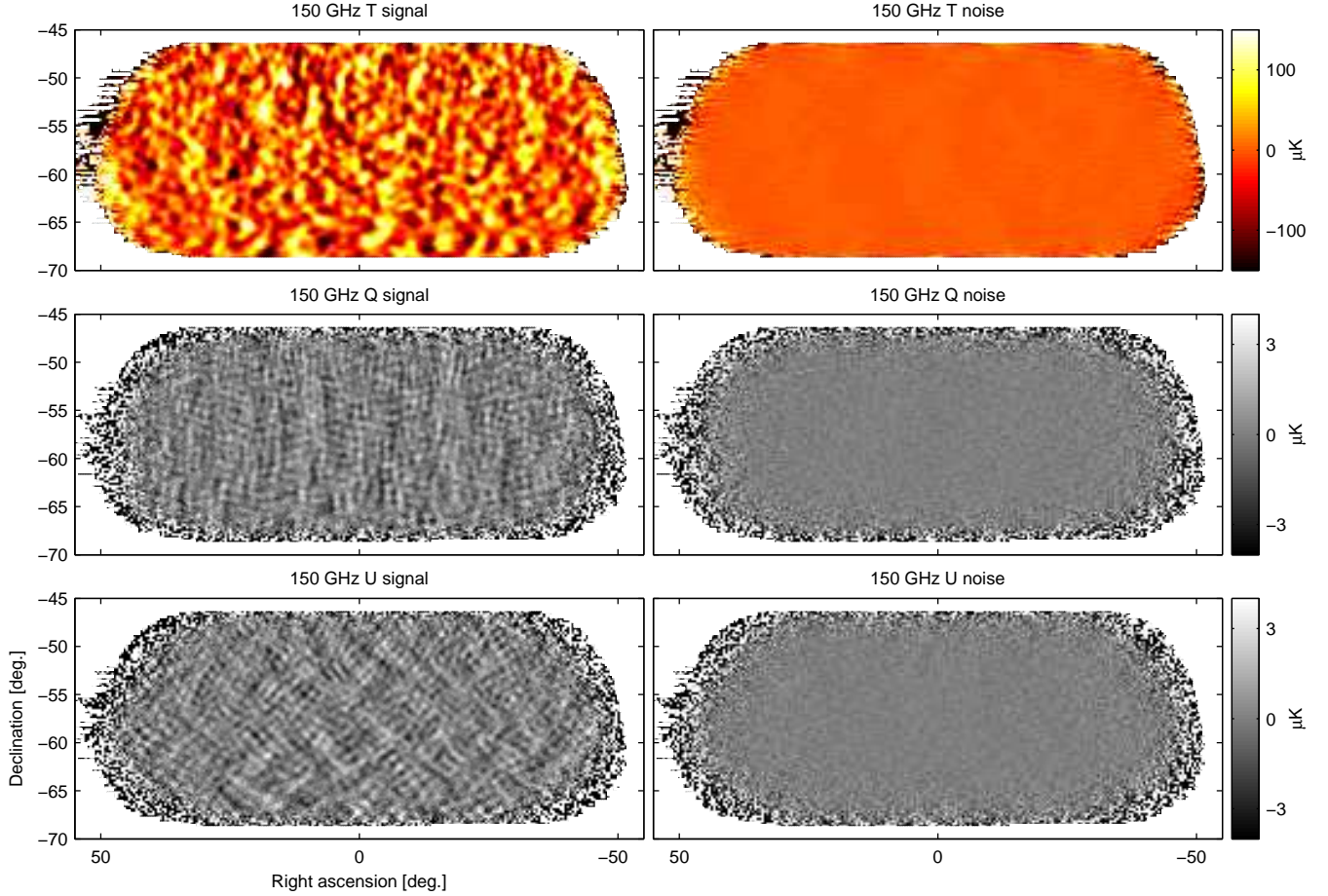
FIG. 9. T, Q, U maps at $150\,\mathrm{GHz}$ using all BICEP2/*Keck* data up to and including that taken during the 2014 observing season—we refer to these maps as BK14$_{150}$. The left column shows the basic signal maps with $0.25°$ pixelization as output by the reduction pipeline. The right column shows a noise realization made by randomly assigning positive and negative signs while coadding the data. These maps are filtered by the instrument beam (FWHM 30 arcmin), timestream processing, and (for Q & U) deprojection of beam systematics. Note that the horizontal/vertical and $45°$ structures seen in the Q and U signal maps are expected for an E-mode dominated sky.

Planck bands resulting in 11 auto and 55 cross-spectra. In Fig. 14 we show all of these together with the baseline lensed-ΛCDM+dust and upper limit lensed-ΛCDM+synchrotron models. Note that, as expected from Fig 8, several spectra contribute to constraining synchrotron.

Fig. 15 shows the distribution of the normalized deviations between the data and the maximum likelihood (ML) model (i.e. data minus expectation value divided by the square root of the diagonal of the bandpower covariance matrix). Since the bandpower distributions are not strictly Gaussian we overplot the same quantity from a set of lensed-ΛCDM+dust+noise simulations evaluated against their input model. (These simulations use the model $A_{d,353} = 3.75\,\mu\mathrm{K}^2$, $\beta_d = 1.59$ and $\alpha_d = -0.42$.) We see one nominally 4.0σ point which is bandpower four of $\mathrm{P}_{217}\times\mathrm{P}_{217}$ (see Fig. 14)—comparing to the simulated distribution this event it not unlikely. Taking χ^2 versus the ML model yields 654, which compared to the distri-

bution from simulations has a PTE of ~ 0.1. We conclude that there is no evidence that the signal or noise models are an inadequate explanation of the data.

Appendix E: Likelihood Variation and Validation

1. Likelihood Evolution

In Fig 5 some evolutionary steps were shown between the previous BKP analysis and the new BK14 analysis presented in this paper. Fig 16 shows some additional detail. The first step is to the alternate analysis including synchrotron which was shown in Fig. 8 of BKP (solid red to dashed-red). This used the BK13 maps plus all of the polarized bands of *Planck* and set $\beta_s = -3.3$ and $\alpha_s = -0.6$. (In BKP the synchrotron pivot frequency was set to $150\,\mathrm{GHz}$ but since a fixed value of β_s was used there we can simply transform the results to the pivot of
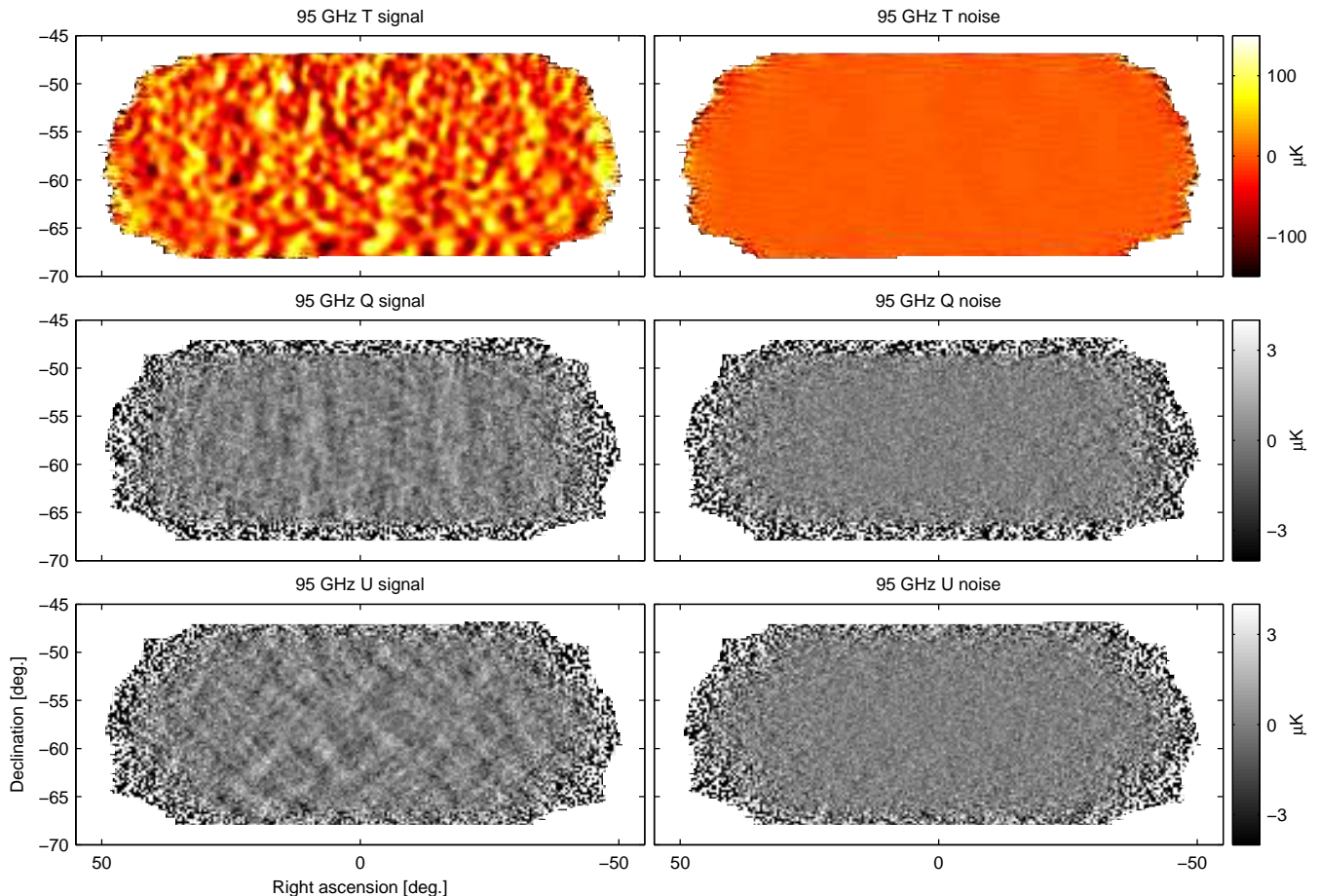
FIG. 10. T, Q, U maps at 95 GHz using data taken by two receivers of *Keck Array* during the 2014 season—we refer to these maps as $BK14_{95}$. These maps are directly analogous to the 150 GHz maps shown in Fig. 9 except that the instrument beam filtering is in this case 43 arcmin FWHM.

23 GHz used in this work.) Next we show the cumulative effects of model changes which we have made for this paper:

We extend the bandpower range from five ($20 < \ell < 200$) to nine ($20 < \ell < 330$) bandpowers—given that lensing is included in the model there is no real reason not to include these additional bandpowers (dashed-red to solid blue). We see that the A_{sync} constraint tightens somewhat.

We switch from the use of *Planck* single-frequency split/split cross-spectra (in this case Y1×Y2) to full map auto spectra (blue to cyan). This is done for technical reasons—substituting in the cross-spectra causes numerical problems in the HL likelihood. The auto spectra have higher signal-to-noise and the constraint on A_{sync} tightens further.

We include the WMAP 23 & 33 GHz bands and see that these have considerable additional power to constrain synchrotron (cyan to magenta).

In BKP we used $\beta_{\mathrm{s}} = -3.3$ as this is the mean value within our field of the "model f" synchrotron spectral index maps available for download from the WMAP website.

site [24]. However that analysis does not distinguish between the spectral behavior of temperature and polarization anisotropy. Ref. [23] analyzed the WMAP data and found a mean value of $\beta_{\mathrm{s}} = -3.1 \pm 0.04$ for polarization at high galactic latitude. In this analysis we use a central value of $\beta_{\mathrm{s}} = -3.1$, and since possible patch-to-patch variation is poorly constrained, to be conservative we marginalize over a Gaussian prior with width $\sigma = 0.3$. More recently Ref. [25] examined the same data and found $\beta_{\mathrm{s}} \approx -3.0$ with considerable fluctuation. This change has very little effect (magenta to yellow).

Polarized synchrotron and dust emission can be spatially correlated—indeed they are guaranteed to be so on the largest scales. Ref. [25] reports a correlation of 0.2 for $30 < \ell < 200$. To be conservative in this analysis we marginalize over the range $0 < \epsilon < 1$. This causes the constraint on synchrotron to tighten because of the non-detection of signal in spectra like $P_{30} \times P_{353}$ (yellow to green). We note that the data prefer the value $\epsilon = 0$ as seen in the upper-right panel of Fig. 4.

In BKP we used $\alpha_{\mathrm{d}} = -0.42$ following the analysis of large regions of high latitude sky in Ref. [9], and $\alpha_{\mathrm{s}} =$
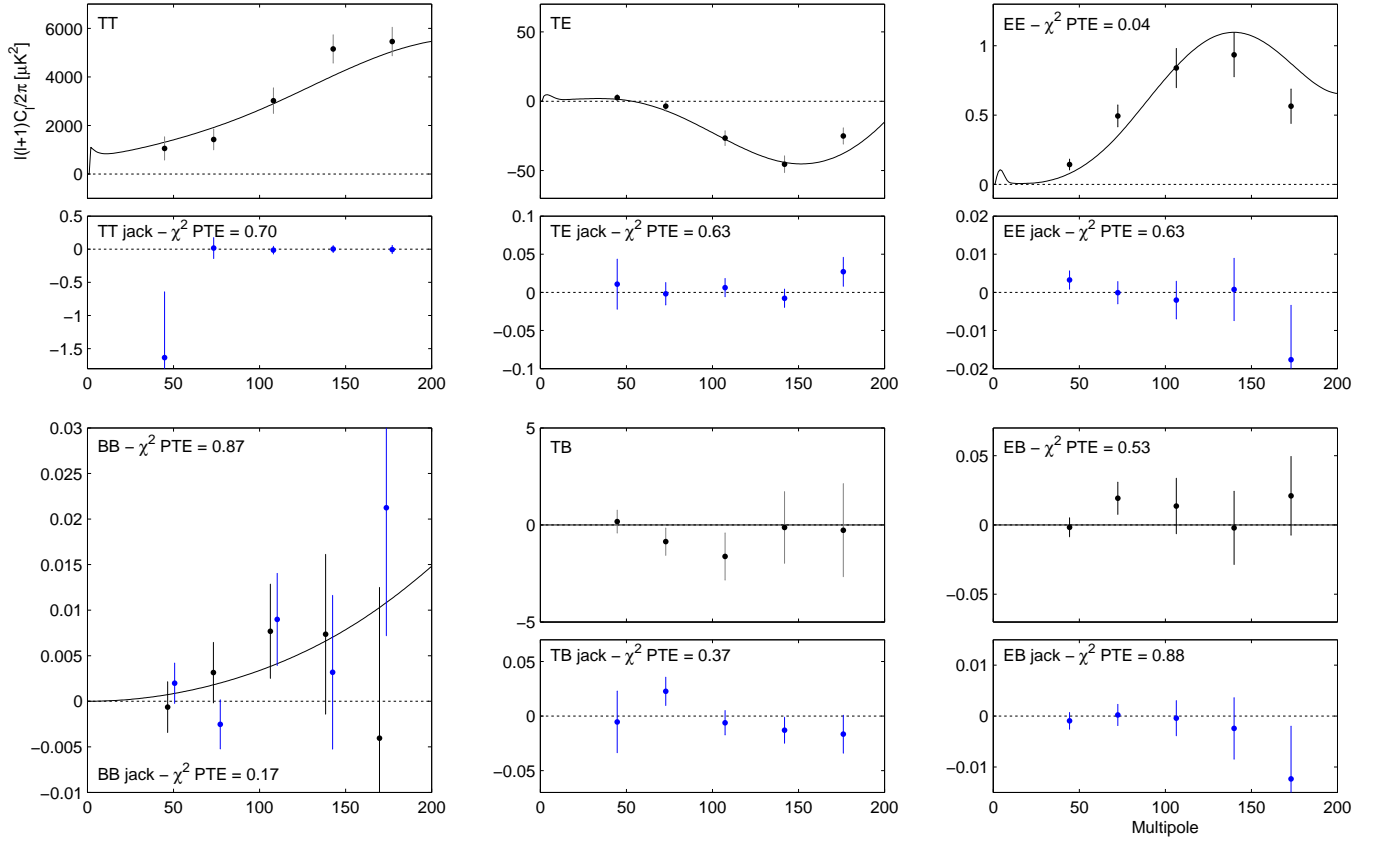
FIG. 11. *Keck Array* power spectrum at 95 GHz for signal (black points) and deck rotation jackknife (blue points). The solid black curves show the lensed-ΛCDM theory spectra. The error bars are the standard deviations of the lensed-ΛCDM+noise simulations and hence contain no sample variance on any additional signal component. The probability to exceed (PTE) the observed value of a simple χ^2 statistic is given (as evaluated against the simulations). Note the very different y-axis scales for the jackknife spectra (other than BB). (Also note that the calibration procedure uses EB to set the overall polarization angle so TB and EB as plotted above cannot be used to measure astrophysical polarization rotation.) This figure is analogous to Fig. 2 of BK-I and Fig. 4 of BK-V.

−0.6 taken from Ref. [26]. In this work we found that we can marginalize over generous ranges in these parameters $-1 < \alpha_\mathrm{d} < 0$ & $-1 < \alpha_\mathrm{s} < 0$ with only a tiny change in the bottom line results so we choose to do so (green to dashed-blue).

Finally we show the changes resulting from adding the new 150 GHz and 95 GHz data (dashed-blue to dashed-black and dashed-black to heavy-black). As already seen in Fig. 5 these are much more significant.

2. Likelihood Variation

In Fig. 17 we investigate several variations to the baseline analysis in terms of the model priors and input data sets. The first four of these loosen the priors and/or remove data, while the final three tighten the priors and/or add data.

First we repeat a variation already shown in Fig. 5— we remove the prior on the frequency spectral index of dust β_d (black to cyan). The data then constrains β_d to a

well behaved, approximately Gaussian range (not shown) with mean/σ of 1.82/0.26. The value of $A_{\mathrm{d},353}$ shifts up slightly but, with the steeper slope versus frequency, the r constraint also shifts up slightly to $r = 0.043^{+0.033}_{-0.031}$ with a zero-to-peak likelihood ratio of 0.44 (10% likely if $r = 0$).

Second we relax the prior on the frequency spectral index of synchrotron to $-4 < \beta_\mathrm{s} < -2$ and see that this has very little effect on any of the curves (black to green).

Third we remove all the *Planck* LFI bands from consideration (black to magenta). This causes the peak of the r constraint to shift down a little and the A_sync constraint to peak quite strongly away from zero, while the A_d constraint is not significantly affected.

Fourth we drop the two bands of WMAP (black to yellow). This slightly decreases the zero-to-peak ratio of the r constraint and significantly tightens the A_sync constraint.

Fifth we switch from $0 < \epsilon < 1$ to the value preferred by Ref. [25] $\epsilon = 0.2$ (black to dashed-red). This makes almost no difference to any of the constraints.
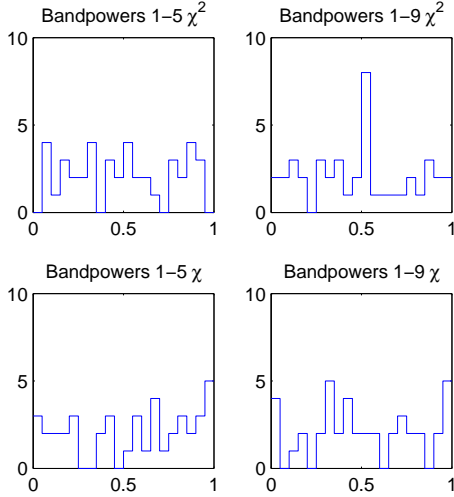
FIG. 12. Distributions of the jackknife χ^2 and χ PTE values for the *Keck Array* 2014 95 GHz data over the tests and spectra given in Table I. This figure is analogous to Fig. 4 of BK-I and Fig. 6 of BK-V.

Sixth we include all the EE and EB spectra under the assumption that the EE/BB ratios for dust and synchrotron are exactly 2 (black to dashed-black). For dust this ratio was found to apply when averaging over large areas of sky in Ref. [9]. Ref. [25] states that this ratio also applies on average for synchrotron. Assuming this fixed ratio leads to extra constraining power—the r curve shifts up slightly, the A_{d} curve narrows and the A_{sync} curve peaks strongly away from zero. It is unclear how much patch-to-patch variation we should in fact allow in the EE/BB ratio so this variation should not be over interpreted at this time.

3. Likelihood Validation

As already mentioned we run full timestream simulations of a lensed-ΛCDM+dust model ($A_{d,353} = 3.75\,\mu\mathrm{K}^2$, $\beta_d = 1.59$ and $\alpha_d = -0.42$). We would like to check that the HL likelihood as implemented is capable of recovering the input values of this model. However if we run the standard COSMOMC analysis on these we of course find that the ML values are biased, since only zero or positive values of r and A_{sync} are allowed. We therefore instead run a ML search on each sim realization where the values of r and A_{sync} are artificially allowed to go negative (as is A_{d} although in practice it doesn't). Fig. 18 shows the results—the input values are recovered in the mean as expected.

An additional piece of information which comes from this study is the standard deviation of the recovered ML r parameter, $\sigma(r) = 0.024$. Unlike the width of the

68% highest posterior density intervals derived from the marginalized r curve shown in Fig. 4 and quoted with
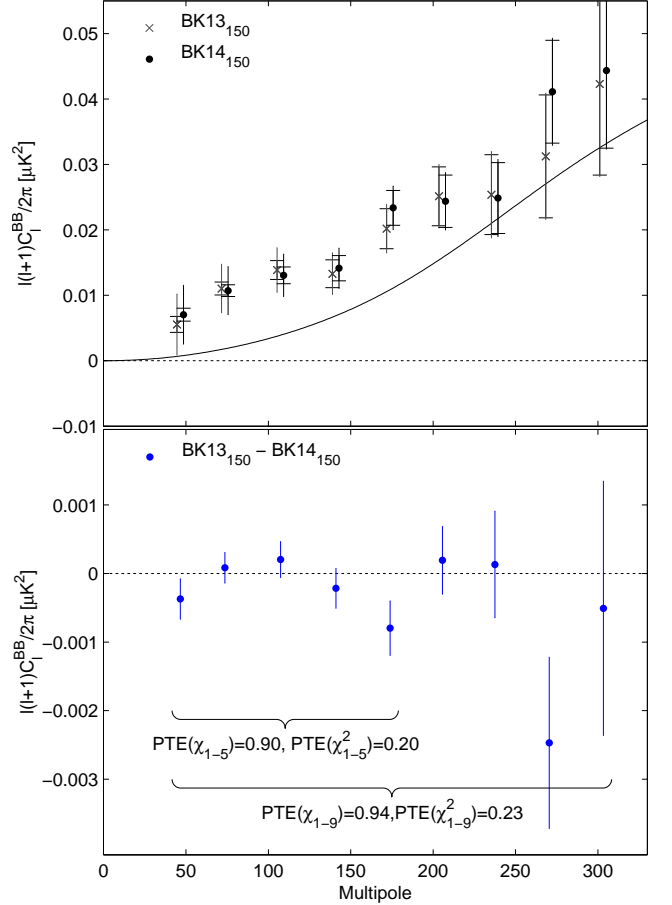

FIG. 13. *Upper:* Comparison of the 150 GHz BB auto-spectrum as previously published (BK13$_{150}$), and with the addition of data taken during 2014 (BK14$_{150}$). The inner error bars are the standard deviation of the lensed-ΛCDM+noise simulations, while the outer error bars include the additional fluctuation induced by a signal contribution matching the excess above lensing seen in the data. Note that neither of these uncertainties are appropriate for comparison of the band power values—for this see the lower panel. (For clarity both sets of points are offset horizontally.) *Lower:* The difference of the two spectra shown in the upper panel divided by a factor of four. The error bars are the standard deviation of the pairwise differences of signal+noise simulations which share common input skies (the simulations used to derive the outer error bars in the upper panel). Comparison of these points with null is an appropriate test of the compatibility of the spectra. This figure is similar to Fig. 8 of BK-V.

our baseline results, this $\sigma(r)$ statistic is insensitive to where the peak value preferred by the data happens to lie, and is therefore a more robust measure of the intrinsic constraining power of the experimental data.

FIG. 14. BB auto- and cross-spectra between the BK14 95 & 150 GHz maps and bands of WMAP and *Planck*. In all cases the quantity plotted is $\ell\,(\ell+1)\,C_l/2\pi\ (\mu K^2)$, and the black curves show the lensed-ΛCDM theory spectrum. The error bars are the standard deviations of the lensed-ΛCDM+noise simulations and hence contain no sample variance on any additional signal component. The blue dashed lines show a baseline lensed-ΛCDM+dust model ($A_{d,353} = 4.3\,\mu K^2$, $\beta_d = 1.6$, $\alpha_d = -0.4$). The red dashed lines show an upper limit lensed-ΛCDM+synchrotron model ($A_{sync,23} = 3.8\,\mu K^2$, $\beta_s = -3.1$, $\alpha_s = -0.6$).
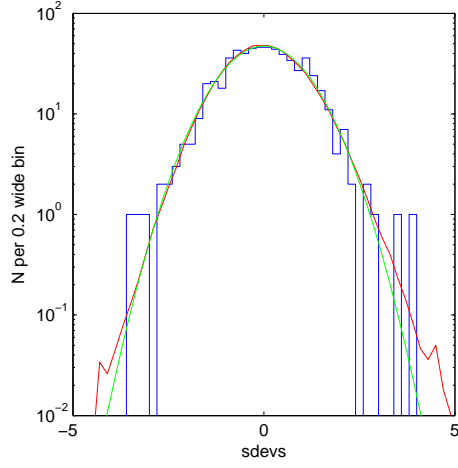
FIG. 15. The normalized deviations of the bandpowers shown in Fig. 14 from the maximum likelihood model is shown as the blue histogram. The red curve is the same thing accumulated over 499 sims of a lensed-ΛCDM+dust model, and the green curve shows a Gaussian with unit width.
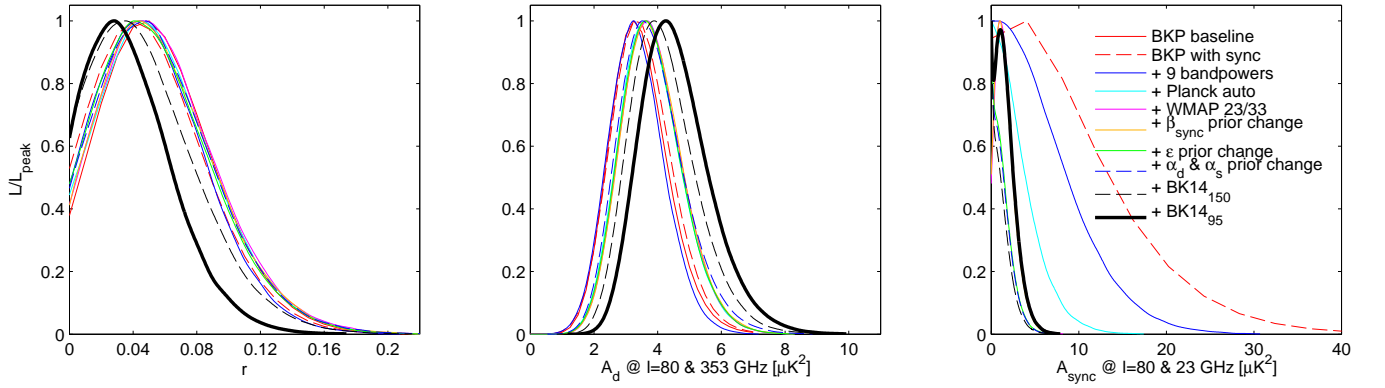

FIG. 16. Evolution of the BKP analysis to the "baseline" analysis as defined in this paper—see Appendix E 1 for details.
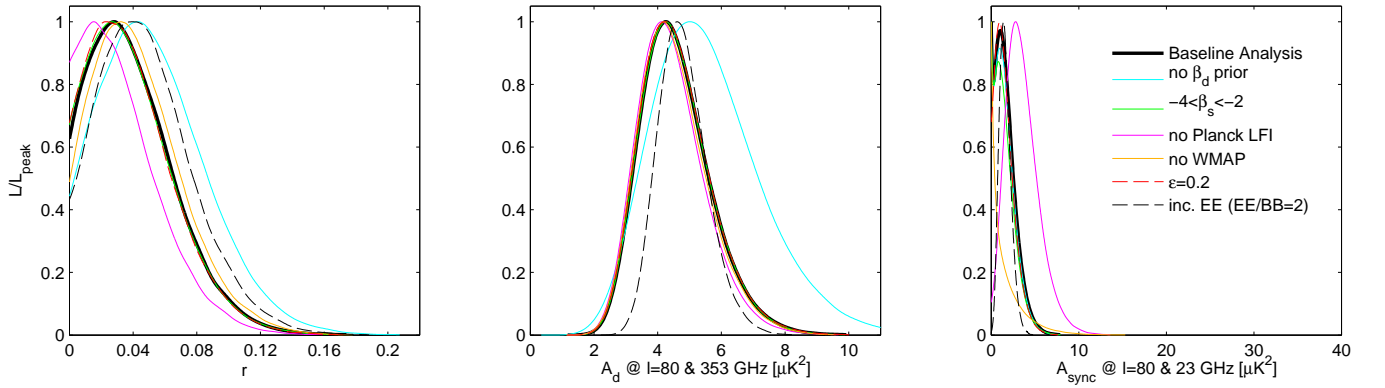

FIG. 17. Likelihood results when varying the data sets and the model priors—see Appendix E 2 for details.
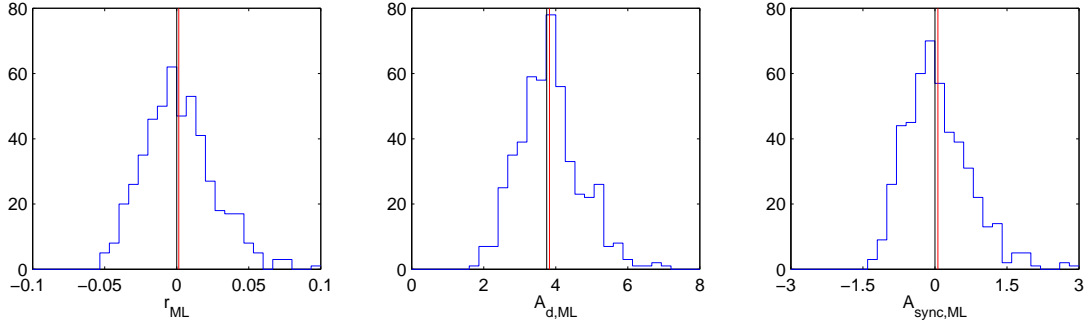
FIG. 18. Results of validation tests running the likelihood on simulations of a lensed-ΛCDM+dust model ($A_{d,353} = 3.75\,\mu\text{K}^2$, $\beta_d = 1.59$ and $\alpha_d = -0.42$). The blue histograms are the recovered ML values with the red line marking their means. The black line shows the input value. In the left panel $\sigma(r) = 0.024$. See Appendix E 3 for details.